LANGMUIR

pubs.acs.org/Langmuir Article

Architecture-Driven Fast Droplet Transport without Mass Loss

Kai Zhuang, Yao Lu, Xiaolei Wang, and Xiaolong Yang*

Cite This: https://doi.org/10.1021/acs.langmuir.1c01608 Read Online

ACCESS | Metrics & More | Article Recommendations | Supporting Information

ABSTRACT: Spontaneous droplet transport without mass loss has great potential applications in the fields of energy and biotechnology, but it remains challenging due to the difficulty in obtaining a sufficient driving force for the transport while suppressing droplet mass loss. Learning from the slippery peristome of *Nepenthes alata* and wedge topology of a shorebird beak that can spontaneously feed water against gravity, a combined system consisting of two face-to-face hydrophilic slippery liquid-infused porous surfaces (SLIPS) with variable beak-like opening and spacing was proposed to constrain the droplet in-between and initiate fast droplet transport over a long distance of 75 mm with a maximum speed of 12.2 mm·s^{-1} without mass loss by taking advantage of the Laplace pressure gradient induced by the asymmetric shape of the constrained droplet. The theoretical model based on the Navier−Stokes equation was developed to interpret the corresponding mechanism of the droplet transport process. In addition, in situ sophisticated droplet manipulations such as droplet mixing are readily feasible when applying flexible 304 stainless foil as the substrate of SLIPS. It is believed that extended research would contribute to new references for the precise and fast droplet motion control intended for energy harvest and water collection devices.

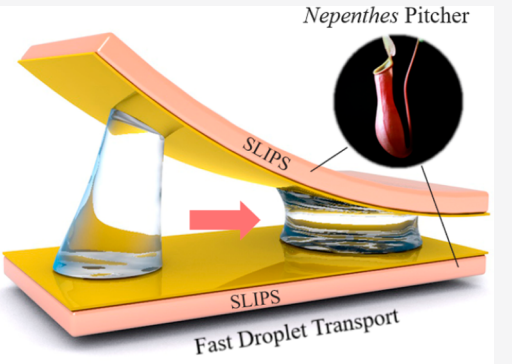

Downloaded via NANJING UNIV AERONAUTICS & ASTRNTICS on October 5, 2021 at 07:58:57 (UTC).
See https://pubs.acs.org/sharingguidelines for options on how to legitimately share published articles.

INTRODUCTION

Droplet motion control has always been a crucial subject of great concern to researchers due to the potential applications in the fields of energy, medicine, and biotechnology.[1−8] The inspiration for reaching this purpose comes from nature, where parts of many creatures, such as spider silk,[9] rice leaves,[10] the back of a desert beetle,[11] the beak of a shorebird,[12,13] and the peristome surface of *Nepenthes*,[14,15] possess the unique capability of holding and transporting water droplets. The key to achieving spontaneous fast droplet transport is to increase the driving force and suppress the moving resistance. Superhydrophobic surfaces (surface with a water contact angle higher than 150°) that mimic the lotus leaf and slippery liquid-infused porous surfaces (SLIPS) inspired by *Nepenthes* pitcher plants have been intensively applied for droplet motion control.[16−25] Although water droplets move easily on the above two kinds of functional surfaces, the interaction between droplets and substrates is completely different. Droplets can be suspended on superhydrophobic surfaces and bead up due to the air cushion beneath that reduces liquid−solid interactions. As a result, the sliding resistance is ultrasmall. When patterns with wettability contrast were introduced on the superhydrophobic surface, droplets would be pinned and slide precisely along the pattern with the aid of gravity.[26,27] Exquisite design of asymmetrical patterns such as wedge-shaped patterns to produce the Laplace pressure gradient for spontaneous droplet transport has also been achieved by numerous studies.[28,29] However, the droplet is likely to retain the patterns and cause contamination. In addition, other external stimulus, such as electricity, optical, *etc.*, can be introduced to the superhydrophobic surface to realize the sophisticated droplet manipulation without mass loss.[30−32] Nonetheless, stimulus-responsive superhydrophobic surfaces involved the external elements which are not suitable for mild biomedical applications or engineering conditions where the stimulus cannot reach. On the contrary, droplet motion on SLIPS is dependent on the liquid−liquid interface between the droplet and the infused lubricant film.[33] Thus, water droplets dispensed on the SLIPS have large footprints and achieve low sliding resistance. Although it is feasible to realize the water droplet motion control by introducing the pattern of wettability contrast on the SLIPS,[34] manipulating the topology of liquid-lubricant interface could be a better choice because there is no mass loss in the process of droplet transport.[35−38] For example, Ruiz-Gutiérrez et al. used silicone oil-infused SLIPS with V-shaped channels to promote the droplet transport and positioning.[35] They also reported the bidirectional motion of the droplet barrel within a wedge-shaped space composed of two hydrophobic SLIPS and conducted theoretical investigations which were important outcomes and formulated a general framework to inspire the design of self-

Received: June 16, 2021
Revised: September 21, 2021

© XXXX American Chemical Society

https://doi.org/10.1021/acs.langmuir.1c01608
Langmuir XXXX, XXX, XXX−XXX

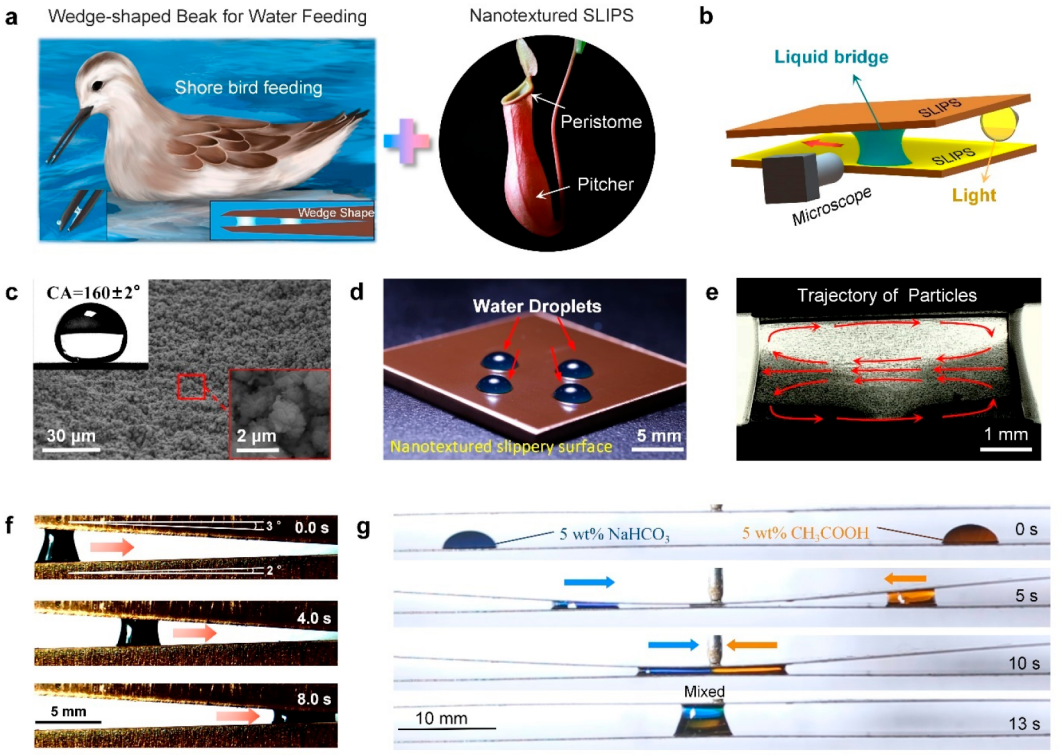

Figure 1. Construction of the multibioinspired system with the structure of the shorebird beak and *Nepenthes alata*: (a) a shorebird feeding water with an opening wedge-shaped beak and a *Nepenthes* pitcher plant with a slippery peristome. (b) Schematic of the droplet transport system with the structure of the shorebird beak and *Nepenthes alata*. (c) SEM images of nanotextured SLIPS before lubricant infusing. (d) Digital photo of the nanotextured SLIPS infused with HTPDMS with 15 μL water droplets on it. (e) Trajectories of graphite particles measured relative to the water droplet reveal that the liquid bridge moves toward the narrowing side accompanied by the rotation. (f) Sliding of 15 μL of water droplet transport between two beak-like SLIPS. (g) Time-lapse photos of the mixing between two 10 μL liquid droplets which are respectively made of a 5 wt % $NaHCO_3$ solution and a 5 wt % CH_3COOH solution.

propelled droplet transport.[36,37] However, the droplet constrained in-between the wedge-shaped space of two hydrophobic SLIPS moves slowly and tends to stop at an equivalent position where the driving force equals the sliding resistance, which manifests the difficulty of long-distance droplet transport. Although the use of the wedge-shaped structure combined with the Leidenfrost effect can initiate ultrafast droplet self-propulsion, the surface temperature needs to be carefully manipulated, and it is not applicable for controlled long-term transport because of the evaporation of the liquid droplets.[39−41]

Here, we demonstrate that the combination of the structure of the slippery peristome of *Nepenthes alata* and wedge topology of the shorebird beak enables rapid, spontaneous droplet transport without mass loss. Two face-to-face hydrophilic SLIPS (the surface with water contact angle less than 90°) with variable beak-like opening and spacing were proposed to constrain the water droplet in-between and initiate fast droplet transport over a long distance of 75 mm with a maximum speed of 12.2 mm·s^{-1} which results from the ultralow sliding resistance of SLIPS and the Laplace pressure gradient induced by the asymmetric shape of liquid bridge. Meanwhile, in situ sophisticated droplet manipulations such as droplet mixing are readily feasible when applying flexible stainless foil as the substrate of SLIPS. In addition, the main factors that determine the velocity of the constrained droplet, such as SLIPS wettability, beak-like opening angle, and spacing distance (the distance between the center of upper and lower SLIPS) of two face-to-face SLIPS, were also discussed with a physical model. The quantitative analysis that consists of the theoretical model and experiments would provide new ideas for spontaneous droplet transport, and the system which combines the peristome surface of *Nepenthes alata* with the wedge-shaped shorebird beak would contribute to new references for the precise and fast droplet motion control intended for energy harvest and water collection devices.

MATERIALS AND METHODS

Materials. Copper sheets (30 mm× 30 mm × 2 mm) and stainless steel foil (100 mm × 12 mm × 0.5 mm) were purchased from Suzhou Metal Material Manufacturer (China). Fluoroalkylsilane [FAS, $C_8F_{13}H_4Si(OCH_2CH_3)_3$] and hydroxy-terminated polydimethylsiloxane (HTPDMS, surface tension γ = 29 mN·m^{-1}) were purchased from Macklin Co., Ltd. (China). 1-Butyl-3-methylimidazolium bis(trifluoromethylsulfonyl)imide (BMI-TFSI, surface tension γ = 40 mN·m^{-1}) was purchased from Monlis Chem. Eng. Sci. & Tech. (Shanghai) Co., Ltd. Fluorinert FC-40 (surface tension γ = 16 mN·m^{-1}) was purchased from Shenzhen China Fluorine Technology Co., Ltd. All chemicals are analytically pure and were used as-received. Steering engines were purchased from Dongguan City Dsservo Technology Co., Ltd. The steering gear model is DS3218, driven by pulse width modulation, and the rotation accuracy can reach ∼ 0.3°. The linear guideway was purchased from Ouli Transmission Co., Ltd. The model of the linear guideway is GX80, and the accuracy of transmission is 0.03 mm.

Fabrication of Nanotextured SLIPS. The entire surfaces of polished copper sheets and stainless steel foil were first milled by using a UV laser marking machine (KY-M-UV3L, Wuhan Keyi, China) with a high speed of 1500 mm·s^{-1}. Then, the samples were immersed in 1 wt % ethanol solution with fluoroalkylsilane [FAS,

https://doi.org/10.1021/acs.langmuir.1c01608
Langmuir XXXX, XXX, XXX−XXX

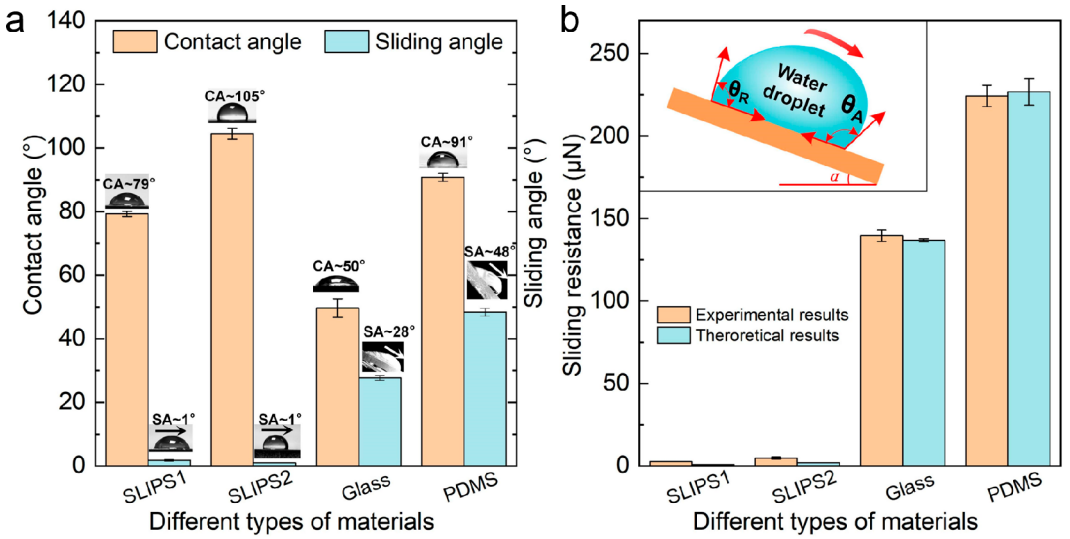

Figure 2. Wettability of droplets on different surfaces: (a) The contact angles and sliding angles of a 30 μL water droplet on four kinds of materials: SLIPS1 (infused with the lubricant of HTPDMS), SLIPS2 (infused with the lubricant of 3 M Fluorinert FC-40), glass, and PDMS (polydimethylsiloxane). (b) Experimental and theoretical sliding resistances of a 30 μL water droplet on the above four kinds of surfaces.

$C_8F_{13}H_4Si(OCH_2CH_3)_3$] for 90 min to lower the surface energy and dried at 120 °C for 30 min. Homogeneous SLIPS can then be obtained by infusing lubricant oil on the as-prepared surface which was tilted at ~45° and held still for 3 h to drain away extra floating oil (Figure S1). SLIPS were infused with HTPDMS (density ρ = 0.9 g·cm^{-3}) and 3 M Fluorinert FC-40 (density ρ = 1.85 g·cm^{-3}) which were referred to as SLIPS1 and SLIPS2, respectively. The mass of the remaining lubricant oil was measured with a precision electronic balance, and the thicknesses of the lubricant were estimated by assuming a uniform lubricant thickness over the area of the sample. The thicknesses of the two kinds of lubricant, HTPDMS and 3 M Fluorinert FC-40, were ~17.7 μm and ~20.3 μm, respectively, which were calculated by the density formula.

Construction of the Multibioinspired System of the Fast Droplet Transport. First, the two steering gears were installed on the stainless steel rails, and then, the rails were aligned horizontally and fixed on the optical platform. The two as-prepared SLIPS (30 mm × 30 mm × 2 mm) were glued to the rotating shafts of the steering gears, and the opening angle and spacing distance between the two face-to-face plates can be precisely controlled by the PC terminal program (Figure S2).

Characterization. Micromorphology of as-prepared surfaces was analyzed using a scanning electron microscope (SEM, Ultra-60, Zeiss, Germany) and a digital microscope (VHX-600, Keyence, Japan). Static and dynamic contact angles were characterized with a goniometer (Rame-Hart 290, USA). Sliding angles were measured with a vertically mounted rotary table. Sliding resistance was obtained by the measured sliding angles and force equilibrium equation. Images and videos of droplet motion on the SLIPS were taken by a digital camera with a 1000 ftp high-speed recording function (RX100M5, Sony, Japan). The mass of the remaining lubricant was measured with a precision electronic balance (JB5374-91, Mettler Toledo, Shang-Hai).

RESULTS AND DISCUSSION

Construction of Multibioinspired Beak-Like SLIPS. Inspired by the wedge topology of the shorebird beak and slippery peristome of *Nepenthes alata* as seen in Figure 1a, the multibioinspired system in our work consisted of two face-to-face SLIPS with a variable beak-like opening and spacing to constrain the droplet in-between and initiate fast droplet transport by taking advantage of the Laplace pressure gradient induced by the asymmetric shape of the constrained droplet (Figure 1b).

The SLIPS were constructed by infusing hydroxy-terminated polydimethylsiloxane (HTPDMS, surface tension γ = 29 mN·m^{-1}) into the nanotextured superhydrophobic surface, as the oil preferentially wetted the superhydrophobic nanotextures and formed a homogeneous liquid layer because the lubricating oil has a lower surface tension and a higher capillary force induced by the nanoporous structure than those of water. In this work, the copper surface was subjected to the laser ablation for creating the nanostructure and then was immersed in fluoroalkylsilane for low surface energy modification to achieve stable Cassie-state superhydrophobicity (Figure S3). By taking advantage of the phase explosion, rapid evaporation, and redeposition of the solid surface produced by laser ablation,[42] a layer of the dense nanospherical structure was formed on the copper surface which could be conducive to help droplets suspend on the surface with the small liquid−solid interface, and 10 μL of the water droplet dispensed on the as-prepared surface had a contact angle of ~160°, as seen in Figure 1c. After infusing with lubricant oil (Figure S3), the liquid−solid interface of a droplet on superhydrophobic surfaces was transited into the liquid−liquid interaction with ultralow sliding resistance. A 15 μL water droplet dispensed on the as-prepared SLIPS infused with HTPDMS has a contact angle of ~79° and a sliding angle of ~1°, exhibiting excellent static stability and dynamic sliding property (Figure 1d and Movie S1). In addition, the process of a 5 μL water droplet mixed with a fluorescent agent sliding across the SLIPS was observed by a microscope with the magnification of 100× lens (Figure S4). Filmed images showed no obvious fluorescent residue along the sliding trace of the droplet, which implied no mass loss occurred in the process of droplet transport (Movie S2).

To construct the shorebird beak-like topology (wedge-shaped opening) (Figure 1a), a platform was built to control the opening angle (0°−180°) and spacing distance (0 mm−50 mm) of the two face-to-face SLIPS so that the liquid bridge can be constrained in-between (Figures 1b and S3). The shape of the liquid bridge is asymmetrical with different curvatures at

https://doi.org/10.1021/acs.langmuir.1c01608
Langmuir XXXX, XXX, XXX−XXX

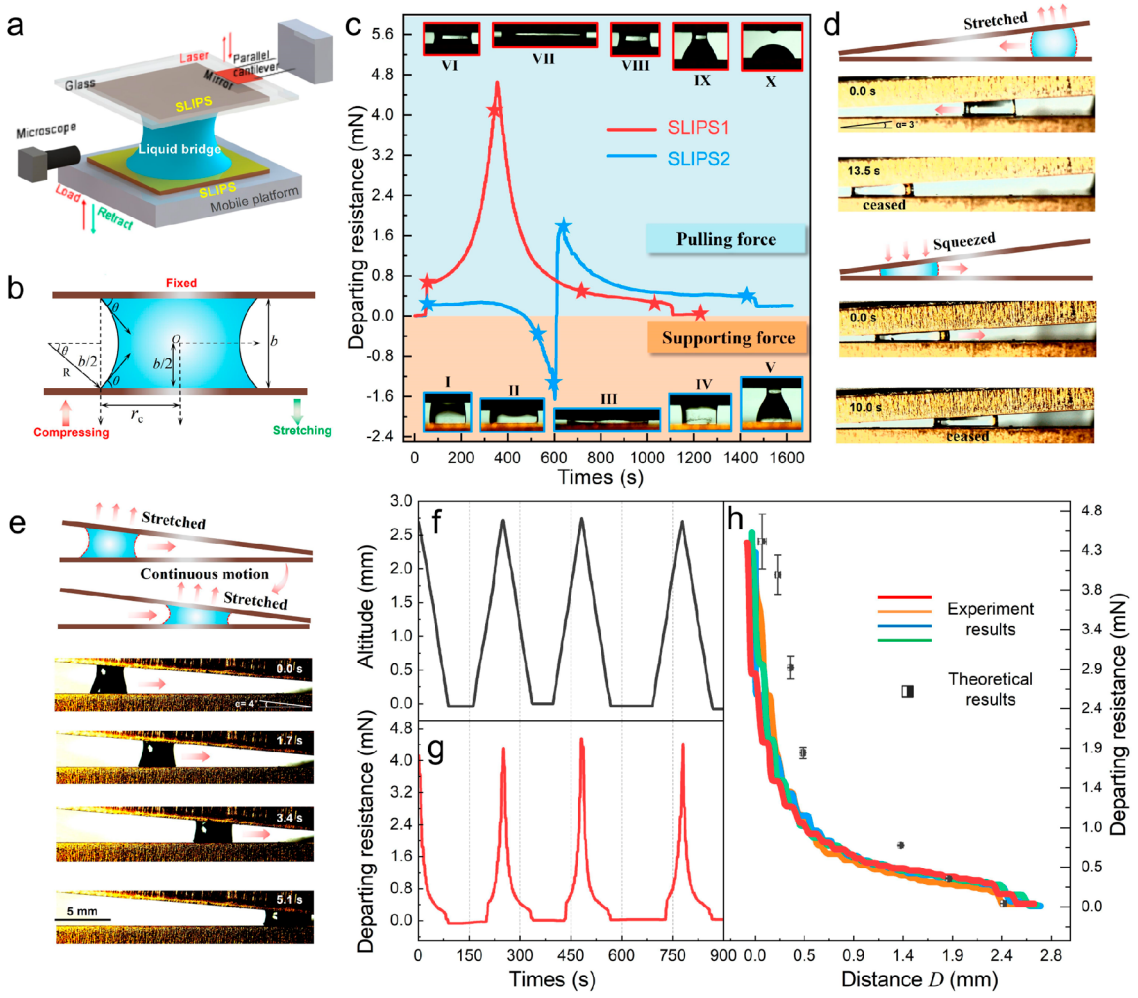

Figure 3. How wettability affects the constrained droplet motion: (a) Schematic of apparatus to measure the departing resistance perpendicular to the contact interface between the droplet and the SLIPS. (b) Schematic of the droplet bridge between the two parallel SLIPS1. (c) Perpendicular departing resistances of a 10 μL water droplet between two face-to-face hydrophilic SLIPS (SLIPS1) and hydrophobic SLIPS (SLIPS2) as a function of time (the five red symbols represent the state of the constrained droplets between two face-to-face hydrophilic SLIPS (SLIPS1) in the inserted images VI–X, respectively, and the blue symbols from left to right represent the state of the constrained droplets between two face-to-face hydrophobic SLIPS (SLIPS2) in the inserted images I–V, respectively). (d) Time-lapse photos of the bidirectional motion of a 20 μL liquid barrel between the two beak-like SLIPS2. (e) Time-lapse series of the continuous directional motion of a 15 μL liquid bridge between the two beak-like SLIPS1. (f) Altitude of the lower plate and (g) departing resistance as a function of time over the process of multicycle dynamic departing resistance measurements. (h) Experimental and modeled departing resistance as a function of the distance (D) between the two face-to-face SLIPS over the process of multicycle dynamic departing resistance measurements.

two flanks, resulting in uneven Laplace pressure inside the droplet and therefore directional movements. As seen in Figure 1e, when the liquid bridge formed in the wedge-shaped beak-like space between the two SLIPS, directional droplet transport is initiated, and the trajectories of mixed graphite particles motion in the liquid bridge were tracked with a high-speed camera. The results showed that two inner convection flows induced by the viscous effect were created inside, which was manifested by the intermediate flow moving forward, driving the upper and lower boundary flows (Movie S3). The laminar flow occurred in the liquid bridge, and the flow pointed to the direction of droplet motion, which is consistent with the simulation results reported by Ruiz-Gutiérrez et al.[38,43] The liquid bridge formed by the 15 μL water droplet moved toward the narrowing side between the two beak-like SLIPS, and the opening angle between the SLIPS is 5° (the opening angle is the sum of the tilt angles of upper SLIPS and lower SLIPS which are 3° and 2°, respectively) (Figure 1f and Movie S4). Furthermore, the bioinspired configuration can realize in situ sophisticated droplet manipulations, such as mixing of microdroplets. As seen in Figure 1g, the flexible 304 stainless steel foil with good elasticity was used as the substrate of SLIPS, as the substrate can spring back without obvious deformation, which is important for in situ reversible droplet manipulations (Figure S5). When pressure was applied on the upper foil SLIPS, reversible sag deformation occurred, and two 10 μL liquid bridges (5 wt % $NaHCO_3$ solution and 5 wt % CH_3COOH solution) dispensed at both edges were transported toward the middle for mixing simultaneously (Movie S5).

Wettability-Dependent Droplet Motion. To clarify the droplet dynamic behavior on the SLIPS, the wettability of hydrophilic (glass) and hydrophobic solid surfaces (polydimethylsiloxane, PDMS) was compared with hydrophilic SLIPS infused with HTPDMS (referred to as SLIPS1) and hydrophobic SLIPS infused with 3 M Fluorinert FC-40

https://doi.org/10.1021/acs.langmuir.1c01608
Langmuir XXXX, XXX, XXX−XXX

(surface tension γ = 16 mN·m^{-1}) (referred to as SLIPS2). The contact angles and sliding angles of 30 μL water droplets on different solid surfaces were measured (Figure 2a). Although the water contact angles of the SLIPS1 and SLIPS2 were slightly larger than those of glass and PDMS, the water sliding angles of SLIPS1 and SLIPS2 were ∼1° which are much smaller than those of the ordinary solid surfaces such as glass and PDMS. The distinct difference of the sliding angles is ascribed to the liquid−liquid interface of SLIPS. The droplet on the PDMS surface remained pinned even at an inclination of 45°, indicating the large sliding resistance of the surface. The sliding resistance was obtained according to force equilibrium

$$F_{re} = mg\cdot\sin\alpha \quad (1)$$

where m is the droplet mass, g is the acceleration of gravity, and α is the measured sliding angle.

In addition to being expressed in terms of components of gravity, the sliding resistance could be well-described by a classical dragging resistance model, which is known as the Furmidge equation[44−47]

$$F_{re} = \gamma\cdot W_{dp}(\cos\theta_R - \cos\theta_A) \quad (2)$$

where γ is the surface tension coefficient of the interface between the droplet and surrounding medium, W_{dp} is the interfacial width of the droplet perpendicular to the sliding direction, while θ_R and θ_A represent receding and advancing contact angles, respectively. The calculated results of the two formulations were compared in Figure 2b, which demonstrated good agreement. From eq 2, it can be inferred that the differences in the advancing and receding contact angles are particularly important factors that affect the droplet sliding resistance on the solid surface, and the sliding resistance increases with the contact angle hysteresis (difference between advancing and receding contact angles). The water droplet on the SLIPS can slide easily with low contact angle hysteresis, which implies that a weak force is enough to drive the constrained droplet between the two beak-like SLIPS.

In addition to the ultralow along-surface sliding resistances of a water droplet on SLIPS, the departing resistance of constrained droplets between two parallel face-to-face SLIPS was also explored to illustrate how the wettability affects the constrained droplet motion. First, departing resistances perpendicular to the droplet footprint were measured with an advanced microforce tester (Figure 3a).[48,49] The SLIPS with dimensions of 10 × 10 mm was fixed upside down on a glass substrate which mounted at the end of a double parallel cantilever with a small mirror. Another identical SLIPS was mounted beneath the upper SLIPS on a mobile platform that can be programmed to rise or fall at a constant speed. Then, a 10 μL water droplet was placed at the center of the lower SLIPS with an initial distance of 10 mm from the upper SLIPS, and the lower surface began to rise at a controlled constant speed of 50 μm·s^{-1}. A CCD camera started to record when the droplet touched the upper SLIPS to form a liquid bridge, and the lower SLIPS kept moving for measuring the supporting force until the upper and lower SLIPS came into contact. Opposite moving was also conducted to measure the departing resistance (Figure 3b and Movie S6). As shown in Figure 3c, the blue curve represented the resistance for the droplet departing from the hydrophobic SLIPS (SLIPS2). Positive results indicated that the surface tension of the constrained droplets produced a pulling force between the two parallel face-to-face SLIPS2 (inserted image I in Figure 3c). As the distance between the two SLIPS2 narrowed, the droplet was gradually squeezed into the shape of a barrel (inserted image II in Figure 3c) with measured resistance gradually decreasing to negative (which means that the pulling force between the two face-to-face SLIPS2 was transited to the supporting force) and then all the way down to −1.65 mN (the maximum supporting force, inserted image III in Figure 3c). As the distance between the two SLIPS2 widened, the supporting force gradually turned back to the pulling force, reaching its maximum of 1.78 mN before finally decreasing to zero when the constrained droplet broke from the SLIPS2. The evolution of the measured force indicated that pulling and supporting forces alternately acted on the two SLIPS2 with one balancing point (0 mN, marked as the equivalent distance) as the distance between the two SLIPS2 varied. As a result, the droplet constrained between two beak-like hydrophobic SLIPS (SLIPS2) would stop at a position with a spacing distance that equals the equivalent distance as seen in Figure 3d. On the contrary, the shape of droplets constrained between the two face-to-face hydrophilic SLIPS (SLIPS1 in Figure 3c) appeared like the liquid bridge with the concave curvature. As shown in the inserted image VI-X in Figure 3c, the force between the two face-to-face hydrophilic SLIPS1 was always above zero (manifesting pulling force), and the maximum obtained pulling force was 4.65 mN, which was 2.6 times larger than that between two hydrophobic SLIPS2 and thus contributed to a much higher average transport velocity of 5.6 mm·s^{-1} (Figure 3e) than the previous data of 0.33 mm·s^{-1}[38] (Movie S7).

To verify the accuracy of the measured microforce between the droplet and SLIPS, four-cycle processes from the formation to the detachment of the liquid bridge between two face-to-face SLIPS1 were recorded by the test program. The altitude of the lower SLIPS1 and the corresponding departing resistance of the upper SLIPS1 are shown in Figures 3f and 3g. The initial point of Figure 3f corresponds to the maximum departing resistance to the upper SLIPS1 when the upper and lower plates stick together. The measured departing resistance is highly repeatable with each load-retract cycle, which indicates that the adhesion capacity of SLIPS1 has great dynamic response characteristics (Figure 3h). The theoretical model was also introduced to calculate the theoretical value of perpendicular departing resistance with formulation 3:[50,51]

$$F_d = F_\gamma + F_{Pcf} \quad (3)$$

Considering the symmetric liquid bridge formed with the contact of two face-to-face identical SLIPS1 (Figure 3b), the departing resistance F_d exerted by the liquid bridge on the upper plate can be simplified as the sum of contributions from the surface tension force F_γ and the fracture capillary force F_{Pcf}. For the upper SLIPS, the surface tension force is directly downward which supports the formation of the liquid bridge. The surface tension force F_γ can be calculated as follows

$$F_\gamma = 2\pi\cdot r_c\cdot\gamma\sin\theta \quad (4)$$

where r_c is the radius of the interface between the liquid bridge and the upper SLIPS plate, γ is the coefficient of water surface tension (72 mN·m^{-1}), and θ is the contact angle of the liquid bridge (Figure 3b).

The fracture capillary force F_{Pcf} on the upper SLIPS plate caused by the concave liquid bridge is induced by the Laplace pressure difference which refers to the difference between the nonwetting phase (gas) pressure and the wetting phase (liquid) pressure. By combining the liquid bridge geometry

https://doi.org/10.1021/acs.langmuir.1c01608
Langmuir XXXX, XXX, XXX−XXX

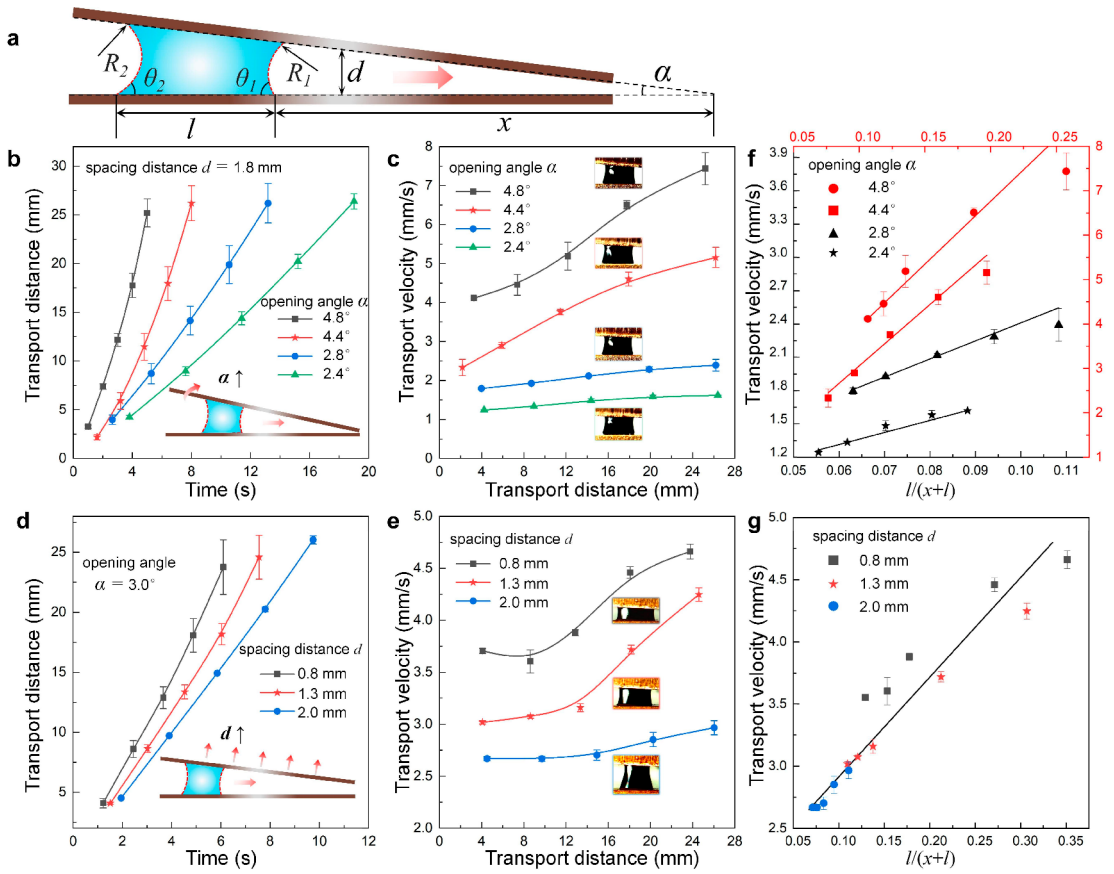

Figure 4. Dynamic analysis of the droplet transport: (a) The schematic of the droplet bridge between the two plates with a beak-like wedge shape. Transport distance of a 15 μL water droplet in-between hydrophilic SLIPS (SLIPS1) as a function of time under the influence of (b) opening angles α and (d) spacing distances d. Transport velocity as a function of transport distance under the influence of (c) opening angles α and (e) spacing distances d. Transport velocity as a function of the value of $l/(l + x)$ under the influence of (f) different opening angles α and (g) different spacing distances d. The spacing distance d in (b, c, f) was 1.8 mm, while the opening angle α in (d, e, g) was 3.0°.

and the fundamental Young−Laplace equation, the fracture capillary force F_{Pcf} can be obtained as below:

$$F_{Pcf} = \pi \cdot r_c^2 \cdot \gamma \cdot \left(\frac{1}{r_c} - \frac{2\cos\theta}{b} \right) \tag{5}$$

The calculated value of F_{pcf} can be negative which means the direction of the fracture force is downward. Thus, the downward direction was set as positive, and when we combined eqs 3, 4, and 5, the departing resistance perpendicular to the upper plate can be obtained with the following final expression:[52]

$$F_{ad} = 2\pi\gamma \cdot r_c \sin\theta + \pi\gamma \cdot r_c^2 \left(\frac{2\cos\theta}{b} - \frac{1}{r_c} \right) \tag{6}$$

The contact angles of the liquid bridge between the upper and lower SLIPS1 are measured and plugged into eq 6 to calculate the theoretical departing resistance, which was compared with the experimental results in Figure 3h. The calculated value of the established theoretical model appears coincidentally with the experimental results. Furthermore, the departing resistances of the water droplet on the hydrophobic SLIPS infused with silicone oil, hydrophilic SLIPS infused with the ionic liquid, and the other ordinary solid surface were also measured in Figure S6. Results indicated that hydrophilic SLIPS showed obvious spatial anisotropy, which meant ultralow along-surface sliding resistance and the ultrahigh perpendicular departing resistance. The lubricant-dependent wettability of SLIPS is an important factor that affects the departing resistance and motion of the constrained droplet between the beak-like SLIPS. Compared with the discontinuous water droplet transport with low velocity between two beak-like hydrophobic SLIPS, hydrophilic SLIPS obviously showed its suitability as a platform for long-distance and fast droplet transport in a beak-like space.

Dynamic Analysis of the Droplet Transport. To further explore the factors affecting droplet velocity between the beak-like SLIPS1, a simplified model was introduced as illustrated in Figure 4a. The two SLIPS1 slope toward each other with the opening angle α, and the lower SLIPS1 is oriented horizontally. The angles θ_1 and θ_2 represent the contact angles corresponding to the right (Edge1) and left (Edge2) edges of the liquid bridge. To describe the position of the liquid bridge in-between, we set x to denote the distance between the right edge of the liquid bridge and the intersection of the two plates and set l to represent the sectional width of the liquid bridge. Due to the asymmetrical heights of the two edges of the liquid bridge and the strong adhesion force exerted on the droplet, different curvatures were formed on Edge1 and Edge2 which were labeled as R_1 and R_2. Edge1 and Edge2 were assumed as circular arcs, and the distortion of the liquid bridge caused by gravity is not considered in this model, as the distance between the two beak-like SLIPS1 is smaller than the capillary length of

https://doi.org/10.1021/acs.langmuir.1c01608
Langmuir XXXX, XXX, XXX−XXX

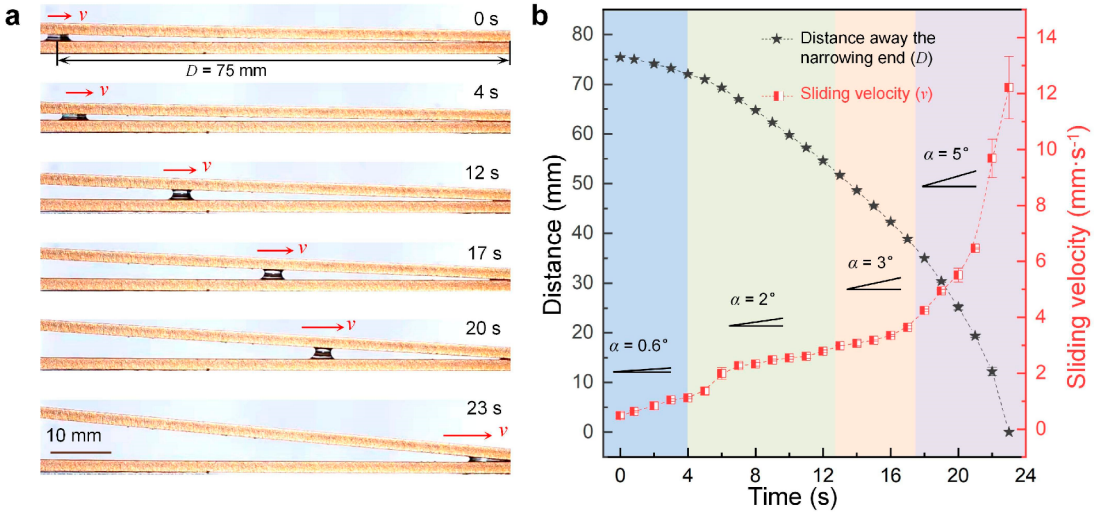

Figure 5. Beak-like architecture-driven long-distance and fast droplet transport: (a) Time-lapse photos of the 5 μL ionic liquid (BMI-TFSI) transport between the two beak-like SLIPS2 (SLIPS infused with 3 M Fluorinert FC-40). (b) Distance between the droplet and narrowing end and sliding velocity of the liquid bridge as a function of time when the opening angle increases from 0.6° to 5.0°.

water (2.7 mm). Based on this assumption, the curvatures R_1 and R_2 can be calculated with the geometric analysis that

$$\frac{1}{R_1} = \frac{\cos\left(\frac{\alpha}{2} - \theta_1\right)}{x \sin\frac{\alpha}{2}} \tag{7}$$

$$\frac{1}{R_2} = \frac{\cos\left(\frac{\alpha}{2} + \theta_2\right)}{(l + x)\sin\frac{\alpha}{2}} \tag{8}$$

The Laplace pressure ΔP at the edge of the liquid bridge can be presented with the difference between the atmospheric pressure P_a and the pressure inside the liquid drop P_i. Subsequently, the Laplace pressure of Edge1 and Edge2 which can be defined as ΔP_1 and ΔP_2, respectively, can be calculated according to the Young−Laplace equation:[53,54]

$$\Delta P_1 = \frac{2\gamma \cos\left(\frac{\alpha}{2} - \theta_1\right)}{x \sin\frac{\alpha}{2}} \tag{9}$$

$$\Delta P_2 = \frac{2\gamma \cos\left(\frac{\alpha}{2} + \theta_2\right)}{(l + x)\sin\frac{\alpha}{2}} \tag{10}$$

Because the liquid−air interface bends toward the interior of liquid, the Laplace pressure points to the air (Figure 3a), and when ΔP_2 is smaller than ΔP_1, the liquid bridge moves to the narrowing end. In the process of transporting the liquid bridge, the contact angles θ_1 and θ_2 are assumed to equal the advancing angle θ_a and the receding angle θ_r of the droplet, respectively. Due to the negligible contact angle hysteresis of SLIPS1, the contact angle θ was used to represent θ_a and θ_r, and in our case, the opening angle α is small. Thus, the difference between ΔP_1 and ΔP_2 can be obtained:

$$\Delta P_1 - \Delta P_2 = \frac{4\gamma \cos\theta}{\alpha}\left(\frac{1}{x} - \frac{1}{l + x}\right) + 2\gamma \sin\theta\left(\frac{1}{x} + \frac{1}{l + x}\right) \tag{11}$$

In our case, the distance between the right of the liquid bridge and the intersection of the two beak-like SLIPS1 is much larger than the length of the sectional liquid bridge ($x \gg l$). Then, the driving force F_d can scale approximately as[55]

$$F_d \approx 2\alpha\gamma l \cdot \sin\theta \tag{12}$$

Eq 12 inferred that the driving force increases with opening angle α and the sectional width l. The subsequent experimental results verified the predicted tendency in the theoretical model, as shown in Figures 4b−4e. When a 15 μL liquid bridge was formed by the constrained water droplet between the two beak-like SLIPS1, the liquid bridge will be transported rapidly to the narrowing side with the aid of the Laplace pressure gradient. The increasing opening angle α will increase the droplet transport velocity when the spacing distance d between the two beak-like SLIPS1 is fixed (Figures 4b and 4c, Movie S8), and when the opening angle α is fixed, the velocity of droplet transport will increase with the decreasing spacing distance d (Figures 4d and 4e, Movie S9). To quantitatively describe the relationship between the droplet transport velocity and other parameters such as opening angle α and the droplet sectional width l, a simplified Navier−Stokes equation was introduced based on two assumptions. First, due to the relatively low droplet velocity and the remarkable laminar structure of the inner flow of the liquid bridge (Figure 1e and Movie S3), the Reynolds number was assumed to be less than 1. Thus, the inertial term in the Navier−Stokes equation was neglected. Second, the motion of the liquid bridge between beak-like SLIPS was one-dimensional along the horizontal direction. Then, the Navier−Stokes equation was deduced as follows[56]

$$\mu\frac{\partial^2 u}{\partial y^2} = \frac{\partial p}{\partial x} \tag{13}$$

where u is the velocity of the liquid bridge, μ is the dynamic viscosity, $\mu(\partial^2 u/\partial y^2)$ represents the viscous force per unit volume along the horizontal direction, p is the liquid pressure, and $\partial p/\partial x$ is the gradient of pressure along the horizontal direction. The viscous term $\mu(\partial^2 u/\partial y^2)$ has an order of magnitude of $\mu(u/\alpha l x)$, and the $\partial p/\partial x$ is approximated as $\Delta p/l$ which is given in eq 11. Accordingly, it can be obtained from eq 13 that

https://doi.org/10.1021/acs.langmuir.1c01608
Langmuir XXXX, XXX, XXX−XXX

$$u \approx k\left(\frac{4\gamma \cos\theta}{\mu}\cdot\frac{l}{x+l} + 2\gamma\alpha \sin\theta\right) \quad (14)$$

where k is a constant determined by experiments. From eq 14, it can be inferred that the transport velocity u linearly increases with $l/(x + l)$, which means that a droplet moves faster at the narrowing end of the beak-like SLIPS. For droplets constrained in the beak-like SLIPS with different opening angles (α = 2.4°, 2.8°, 4.4°, and 4.8°) or spacing distance d (α = 3°), the corresponding velocities of droplets u and $l/(x + l)$ measured in experiments were in linear correlation with different slopes as shown in Figures 4f and 4g which confirmed the great correspondence between the theoretical model and experimental results. Therefore, two ways can be used to improve the velocity of the constrained droplet between the beak-like SLIPS: one is to reduce spacing distance d and to increase the sectional width l of droplet, and the other is to maintain a relatively large opening angle α.

Beak-like Architecture-Driven Long-Distance and Fast Droplet Transport. For a static system, it is contradictory to maintain both large opening angle α and small spacing distance d during the process of droplet transport. To improve the efficiency of droplet transport, it is necessary to make dynamic adjustment for the system, as shown in Figure 5a. The two SLIPS2 were assembled at an opening angle of ~0.6°, the constrained liquid bridge in-between was transported to the narrowing end immediately after releasing, and the transport velocity can be controlled by the opening angle. The opening angle α increased from 0.6° to 5° which enlarged the Laplace pressure gradient and accelerated the droplet sliding. As shown in Figure 5b, the transport velocity increased with increased α and can reach a maximum velocity of 12.2 mm·s^{-1} (Movie S10). In addition, the long-distance transport of a 1 μL microwater droplet could be feasible with the dynamic adjustment of the opening angle (Figure S7).

CONCLUSIONS

A configuration of the multibioinspired system with the structure of the shorebird beak and *Nepenthes alata* was proposed to achieve spontaneous and fast droplet transport without mass loss. The liquid bridge with a concave curvature can be constrained in-between two face-to-face hydrophilic SLIPS with a beak-like wedge opening that was fabricated via a simple laser ablation method. Fast droplet transport over a 75 mm distance can be initiated with a maximum velocity of 12.2 mm·s^{-1} by taking the advantage of the Laplace pressure gradient induced by the asymmetric shape of constrained droplets and the ultralow sliding resistance of SLIPS. After the corresponding experiments and theoretical analysis, the results indicated that the hydrophilic SLIPS was more suitable as a platform for long-distance and fast droplet transport in a beak-like space when compared with the hydrophobic SLIPS. The droplet transport velocity increased with the increase of the opening angle α and with the decrease of spacing distance d, which was validated by experimental results and modeling analysis. In addition, droplet mixing is readily feasible when reversible deformation was applied by using flexible 304 stainless foil as the substrate of SLIPS. More sophisticated droplet manipulations can also have the potential to achieve by in situ distorting the flexible substrates using an external stimulus, such as magnetism, electric, and thermal effects. The design of the system inspired by the wedge topology of the shorebird beak and slippery peristome of *Nepenthes alata* would lend perspective for corresponding potential applications to the fields of energy harvest and water collection devices.

ASSOCIATED CONTENT

Supporting Information

The Supporting Information is available free of charge at https://pubs.acs.org/doi/10.1021/acs.langmuir.1c01608.

Droplet transport between beak-like SLIPS (PDF)

Water droplet sliding on tilted nanotextured SLIPS infused with HTPDMS (SLIPS1) (Movie S1) (MP4)

Water droplet sliding across SLIPS1 without mass loss (Movie S2) (MP4)

Trajectories of graphite particles during droplet transport process (Movie S3) (MP4)

Water droplet bridge sliding between beak-like SLIPS1 (Movie S4) (MP4)

Liquid bridges mixing between two face-to-face SLIPS1 (Movie S5) (MP4)

Deformation of liquid bridge between two parallel face-to-face SLIPS1 and liquid barrel between two parallel face-to-face SLIPS2 (Movie S6) (MP4)

Comparison of directional motion of droplet between beak-like SLIPS1 and bidirectional motion of droplet between beak-like SLIPS2 (Movie S7) (MP4)

Comparison of liquid bridge sliding between beak-like SLIPS1 with different opening angles (Movie S8) (MP4)

Comparison of liquid bridge sliding between beak-like SLIPS1 with different spacing distances (Movie S9) (MP4)

Long-distance liquid bridge transportation between beak-like SLIPS infused with 3 M Fluorinert FC-40 (Movie S10) (MP4)

AUTHOR INFORMATION

Corresponding Author

Xiaolong Yang − *College of Mechanical and Electrical Engineering, Nanjing University of Aeronautics and Astronautics, Nanjing 210016, China; Jiangsu Key Laboratory of Precision and Micro-Manufacturing Technology, Nanjing University of Aeronautics and Astronautics, Nanjing 210016, PR China;* orcid.org/0000-0002-2324-6172; Phone: 86-25-84892551; Email: xlyang@nuaa.edu.cn

Authors

Kai Zhuang − *College of Mechanical and Electrical Engineering, Nanjing University of Aeronautics and Astronautics, Nanjing 210016, China*

Yao Lu − *Department of Chemistry, Queen Mary University of London, London E1 4NS, U.K.;* orcid.org/0000-0001-9566-4122

Xiaolei Wang − *College of Mechanical and Electrical Engineering, Nanjing University of Aeronautics and Astronautics, Nanjing 210016, China*

Complete contact information is available at: https://pubs.acs.org/10.1021/acs.langmuir.1c01608

Author Contributions

K.Z. and Y.L. contributed equally to this work.

https://doi.org/10.1021/acs.langmuir.1c01608
Langmuir XXXX, XXX, XXX−XXX

Notes

The authors declare no competing financial interest.

■ ACKNOWLEDGMENTS

This research was financially supported by the National Natural Science Foundation of China (NSFC, 51905267) and the Natural Science Foundation of Jiangsu Province (BK20192007, BK20190411). Y.L. acknowledges the support from the Royal Society Research Grant (RGS\R1\201071).

■ REFERENCES

(1) Li, J.; Hou, Y.; Liu, Y.; Hao, C.; Li, M.; Chaudhury, M. K.; Yao, S.; Wang, Z. Directional transport of high-temperature Janus droplets mediated by structural topography. *Nat. Phys.* **2016**, *12*, 606−612.
(2) Li, J.; Song, Y.; Zheng, H.; Feng, S.; Xu, W.; Wang, Z. Designing biomimetic liquid diodes. *Soft Matter* **2019**, *15*, 1902−1915.
(3) Ghazimirsaeed, E.; Madadelahi, M.; Dizani, M.; Shamloo, A. Secondary Flows, Mixing, and Chemical Reaction Analysis of Droplet-Based Flow inside Serpentine Microchannels with Different Cross Sections. *Langmuir* **2021**, *37*, 5118−5130.
(4) Villegas, M.; Zhang, Y.; Abu Jarad, N.; Soleymani, L.; Didar, T. F. Liquid-Infused Surfaces: A Review of Theory, Design, and Applications. *ACS Nano* **2019**, *13*, 8517−8536.
(5) Hassan, M. R.; Zhang, J.; Wang, C. Digital Microfluidics: Magnetic Transportation and Coalescence of Sessile Droplets on Hydrophobic Surfaces. *Langmuir* **2021**, *37*, 5823−5837.
(6) Li, J.; Guo, Z. Spontaneous directional transportations of water droplets on surfaces driven by gradient structures. *Nanoscale* **2018**, *10*, 13814−13831.
(7) Zhang, H.; Chen, G.; Yu, Y.; Guo, J.; Tan, Q.; Zhao, Y. Microfluidic Printing of Slippery Textiles for Medical Drainage around Wounds. *Adv. Sci.* **2020**, *7*, 2000789.
(8) Moon, B.-U.; Malic, L.; Morton, K.; Jeyhani, M.; Elmanzalawy, A.; Tsai, S. S. H.; Veres, T. Evaporation-Driven Water-in-Water Droplet Formation. *Langmuir* **2020**, *36*, 14333−14341.
(9) Zheng, Y.; Bai, H.; Huang, Z.; Tian, X.; Nie, F. Q.; Zhao, Y.; Zhai, J.; Jiang, L. Directional water collection on wetted spider silk. *Nature* **2010**, *463*, 640−643.
(10) Wu, D.; Wang, J.-N.; Wu, S.-Z.; Chen, Q.-D.; Zhao, S.; Zhang, H.; Sun, H.-B.; Jiang, L. Three-Level Biomimetic Rice-Leaf Surfaces with Controllable Anisotropic Sliding. *Adv. Funct. Mater.* **2011**, *21*, 2927−2932.
(11) Parker, A. R.; Lawrence, C. R. Water capture by a desert beetle. *Nature* **2001**, *414*, 33−34.
(12) RUBEGA, M. A. Surface tension prey transport in shorebirds: how widespread is it? *Ibis* **1997**, *139*, 488−493.
(13) Prakash, M.; Quere, D.; Bush, J. W. Surface tension transport of prey by feeding shorebirds: the capillary ratchet. *Science* **2008**, *320*, 931−934.
(14) Chen, H.; Zhang, P.; Zhang, L.; Liu, H.; Jiang, Y.; Zhang, D.; Han, Z.; Jiang, L. Continuous directional water transport on the peristome surface of Nepenthes alata. *Nature* **2016**, *532*, 85−89.
(15) Wong, T. S.; Kang, S. H.; Tang, S. K.; Smythe, E. J.; Hatton, B. D.; Grinthal, A.; Aizenberg, J. Bioinspired self-repairing slippery surfaces with pressure-stable omniphobicity. *Nature* **2011**, *477*, 443−447.
(16) Mertaniemi, H.; Jokinen, V.; Sainiemi, L.; Franssila, S.; Marmur, A.; Ikkala, O.; Ras, R. H. Superhydrophobic tracks for low-friction, guided transport of water droplets. *Adv. Mater.* **2011**, *23*, 2911−2914.
(17) Mumm, F.; van Helvoort, A. T. J.; Sikorski, P. Easy Route to Superhydrophobic Copper-Based Wire-Guided Droplet Microfluidic Systems. *ACS Nano* **2009**, *3*, 2647−2652.
(18) Huang, W.-P.; Chen, X.; Hu, M.; Hu, D.-F.; Wang, J.; Li, H.-Y.; Ren, K.-F.; Ji, J. Patterned Slippery Surface through Dynamically Controlling Surface Structures for Droplet Microarray. *Chem. Mater.* **2019**, *31*, 834−841.
(19) Li, X.; Yang, J.; Lv, K.; Papadopoulos, P.; Sun, J.; Wang, D.; Zhao, Y.; Chen, L.; Wang, D.; Wang, Z.; Deng, X. Salvinia-like slippery surface with stable and mobile water/air contact line. *Natl. Sci. Rev.* **2021**, *8*, nwaa153.
(20) Tang, Y.; Yang, X.; Li, Y.; Zhu, D. Design of Hybrid Superwetting Surfaces with Self-Driven Droplet Transport Feature for Enhanced Condensation. *Adv. Mater. Interfaces* **2021**, *8*, 2100284.
(21) Tang, Y.; Yang, X.; Li, Y.; Lu, Y.; Zhu, D. Robust Micro-Nanostructured Superhydrophobic Surfaces for Long-Term Dropwise Condensation. *Nano Lett.* **2021**, DOI: 10.1021/acs.nanolett.1c01584.
(22) Feng, S.; Delannoy, J.; Malod, A.; Zheng, H.; Quéré, D.; Wang, Z. Tip-induced flipping of droplets on Janus pillars: From local reconfiguration to global transport. *Sci. Adv.* **2020**, *6*, eabb4540.
(23) Li, J.; Zhou, X.; Li, J.; Che, L.; Yao, J.; McHale, G.; Chaudhury, M. K.; Wang, Z. Topological liquid diode. *Sci. Adv.* **2017**, *3*, eaao3530.
(24) Sun, Q.; Wang, D.; Li, Y.; Zhang, J.; Ye, S.; Cui, J.; Chen, L.; Wang, Z.; Butt, H.-J.; Vollmer, D.; Deng, X. Surface charge printing for programmed droplet transport. *Nat. Mater.* **2019**, *18*, 936−941.
(25) Xu, W.; Zheng, H.; Liu, Y.; Zhou, X.; Zhang, C.; Song, Y.; Deng, X.; Leung, M.; Yang, Z.; Xu, R. X.; Wang, Z. L.; Zeng, X. C.; Wang, Z. A droplet-based electricity generator with high instantaneous power density. *Nature* **2020**, *578*, 392−396.
(26) Yang, X.; Song, J.; Chen, N.; Liu, X. Open surface multifunctional droplet manipulation platform fabricated by micro-milling. *J. Mater. Sci.* **2019**, *54*, 10715−10727.
(27) Yang, X.; Liu, X.; Lu, Y.; Song, J.; Huang, S.; Zhou, S.; Jin, Z.; Xu, W. Controllable Water Adhesion and Anisotropic Sliding on Patterned Superhydrophobic Surface for Droplet Manipulation. *J. Phys. Chem. C* **2016**, *120*, 7233−7240.
(28) Stamatopoulos, C.; Milionis, A.; Ackerl, N.; Donati, M.; Leudet de la Vallée, P.; Rudolf von Rohr, P.; Poulikakos, D. Droplet Self-Propulsion on Superhydrophobic Microtracks. *ACS Nano* **2020**, *14*, 12895−12904.
(29) Wu, J.; Yin, K.; Li, M.; Wu, Z.; Xiao, S.; Wang, H.; Duan, J.-A.; He, J. Under-oil self-driven and directional transport of water on a femtosecond laser-processed superhydrophilic geometry-gradient structure. *Nanoscale* **2020**, *12*, 4077−4084.
(30) Ichimura, K.; Oh, S. K.; Nakagawa, M. Light-driven motion of liquids on a photoresponsive surface. *Science* **2000**, *288*, 1624−6.
(31) Lv, J.-a.; Liu, Y.; Wei, J.; Chen, E.; Qin, L.; Yu, Y. Photocontrol of fluid slugs in liquid crystal polymer microactuators. *Nature* **2016**, *537*, 179−184.
(32) Li, C.; Guo, R.; Jiang, X.; Hu, S.; Li, L.; Cao, X.; Yang, H.; Song, Y.; Ma, Y.; Jiang, L. Reversible Switching of Water-Droplet Mobility on a Superhydrophobic Surface Based on a Phase Transition of a Side-Chain Liquid-Crystal Polymer. *Adv. Mater.* **2009**, *21*, 4254−4258.
(33) Smith, J. D.; Dhiman, R.; Anand, S.; Reza-Garduno, E.; Cohen, R. E.; McKinley, G. H.; Varanasi, K. K. Droplet mobility on lubricant-impregnated surfaces. *Soft Matter* **2013**, *9*, 1772−1780.
(34) Paulssen, D.; Hardt, S.; Levkin, P. A. Droplet Sorting and Manipulation on Patterned Two-Phase Slippery Lubricant-Infused Surface. *ACS Appl. Mater. Interfaces* **2019**, *11*, 16130−16138.
(35) Guan, J. H.; Ruiz-Gutiérrez, É.; Xu, B. B.; Wood, D.; McHale, G.; Ledesma-Aguilar, R.; Wells, G. G. Drop transport and positioning on lubricant-impregnated surfaces. *Soft Matter* **2017**, *13*, 3404−3410.
(36) Ruiz-Gutiérrez, É.; Guan, J.; Xu, B.; McHale, G.; Wells, G. G.; Ledesma-Aguilar, R. Energy Invariance in Capillary Systems. *Phys. Rev. Lett.* **2017**, *118*, 218003.
(37) Ruiz-Gutiérrez, É.; Semprebon, C.; McHale, G.; Ledesma-Aguilar, R. Statics and dynamics of liquid barrels in wedge geometries. *J. Fluid Mech.* **2018**, *842*, 26−57.
(38) Sadullah, M. S.; Launay, G.; Parle, J.; Ledesma-Aguilar, R.; Gizaw, Y.; McHale, G.; Wells, G. G.; Kusumaatmaja, H. Bidirectional motion of droplets on gradient liquid infused surfaces. *Commun. Phys.* **2020**, *3*, 166.
(39) Luo, C.; Mrinal, M.; Wang, X. Self-propulsion of Leidenfrost Drops between Non-Parallel Structures. *Sci. Rep.* **2017**, *7*, 12018.

https://doi.org/10.1021/acs.langmuir.1c01608
Langmuir XXXX, XXX, XXX−XXX

(40) Agrawal, P.; Wells, G. G.; Ledesma-Aguilar, R.; McHale, G.; Buchoux, A.; Stokes, A.; Sefiane, K. Leidenfrost heat engine: Sustained rotation of levitating rotors on turbine-inspired substrates. *Appl. Energy* **2019**, *240*, 399−408.
(41) Wells, G. G.; Ledesma-Aguilar, R.; McHale, G.; Sefiane, K. A sublimation heat engine. *Nat. Commun.* **2015**, *6*, 6390.
(42) He, H.; Wang, C.; Zhang, X.; Ning, X.; Sun, L. Facile fabrication of multi-scale microgroove textures on Ti-based surface by coupling the re-solidification bulges derived from nanosecond laser irradiation. *Surf. Coat. Technol.* **2020**, *386*, 125460.
(43) Ruiz-Gutiérrez, É.; Ledesma-Aguilar, R. Lattice-Boltzmann simulations of the dynamics of liquid barrels. *J. Phys.: Condens. Matter* **2020**, *32*, 214007.
(44) Yang, X.; Song, J.; Zheng, H.; Deng, X.; Liu, X.; Lu, X.; Sun, J.; Zhao, D. Anisotropic sliding on dual-rail hydrophilic tracks. *Lab Chip* **2017**, *17*, 1041−1050.
(45) Balu, B.; Berry, A. D.; Hess, D. W.; Breedveld, V. Patterning of superhydrophobic paper to control the mobility of micro-liter drops for two-dimensional lab-on-paper applications. *Lab Chip* **2009**, *9*, 3066.
(46) Furmidge, C. Studies at phase interfaces. I. The sliding of liquid drops on solid surfaces and a theory for spray retention. *J. Colloid Sci.* **1962**, *17*, 309−324.
(47) Yang, X.; Zhuang, K.; Lu, Y.; Wang, X. Creation of Topological Ultraslippery Surfaces for Droplet Motion Control. *ACS Nano* **2021**, *15*, 2589−2599.
(48) Li, M.; Jiao, Q.; Dai, Q.; Shi, L.; Huang, W.; Wang, X. Effects of bulk viscoelasticity and surface wetting on the contact and adhesive properties of a soft material. *Polym. Test.* **2019**, *74*, 266−273.
(49) Li, M.; Xie, J.; Shi, L.; Huang, W.; Wang, X. Controlling direct contact force for wet adhesion with different wedged film stabilities. *J. Phys. D: Appl. Phys.* **2018**, *51*, 165305.
(50) Wen, J.; Dini, D.; Reddyhoff, T. Design and optimization of a liquid ring thrust bearing. *Tribol. Int.* **2020**, *149*, 105588.
(51) Dai, Q.; Hu, Z.; Huang, W.; Wang, X. Controlled support of a magnetic fluid at a superhydrophobic interface. *Appl. Phys. Lett.* **2020**, *116*, 221601.
(52) Mahmood, A.; Chen, S.; Chen, L.; Liu, D.; Chen, C.; Weng, D.; Wang, J. Unidirectional transport of water nanodroplets entrapped inside a nonparallel smooth surface: a molecular dynamics simulation study. *RSC Adv.* **2019**, *9*, 41984−41992.
(53) Chen, H.; Tang, T.; Amirfazli, A. Liquid transfer mechanism between two surfaces and the role of contact angles. *Soft Matter* **2014**, *10*, 2503−7.
(54) Luo, C.; Heng, X.; Xiang, M. Behavior of a liquid drop between two nonparallel plates. *Langmuir* **2014**, *30*, 8373−80.
(55) Lei, W.; Hou, G.; Liu, M.; Rong, Q.; Xu, Y. High-speed transport of liquid droplets in magnetic tubular microactuators. *Sci. Adv.* **2018**, *4*, eaau8767.
(56) Heng, X.; Luo, C. Liquid drop runs upward between two nonparallel plates. *Langmuir* **2015**, *31*, 2743−8.

https://doi.org/10.1021/acs.langmuir.1c01608
Langmuir XXXX, XXX, XXX−XXX